Model validation image data for breakup of a liquid jet in crossflow: part I

Sedarsky, David; Paciaroni, Megan; Berrocal, Edouard; Petterson, Per; Zelina, Joseph; Gord, James; Linne, Mark

Published in:
Experiments in Fluids

DOI:
10.1007/s00348-009-0807-2

2010

Document Version:
Publisher's PDF, also known as Version of record

Exp Fluids (2010) 49:391–408
DOI 10.1007/s00348-009-0807-2

RESEARCH ARTICLE

Model validation image data for breakup of a liquid jet in crossflow: part I

David Sedarsky · Megan Paciaroni · Edouard Berrocal · Per Petterson · Joseph Zelina · James Gord · Mark Linne

Received: 2 April 2009 / Revised: 20 December 2009 / Accepted: 23 December 2009 / Published online: 9 January 2010

Abstract We have applied three different imaging diagnostics: particle imaging velocimetry, high-speed shadowgraphy, and ballistic imaging, to observe the breakup of a liquid jet in a crossflow of air under a variety of conditions. The experimental system was designed to provide well-controlled conditions with minimal amounts of turbulence in the liquid jet and the gaseous crossflow. A variety of Weber numbers and momentum flux ratios were studied in order to provide a sizable data set for the validation of computational models. This paper briefly describes the three spray imaging techniques, outlines the results obtained to-date, and tabulates image statistics for each of ten spray conditions at varying distances from the spray nozzle orifice. The end result is a first installment in what will become a comprehensive model validation data set for jets in crossflow for use by computational fluid dynamics modelers.

1 Introduction

Transportation systems are typically powered by liquid fuels because liquids contain much more energy per unit volume than gaseous fuels, and liquids are relatively easy to transport and store using a large and well-established infrastructure. Even if energy supplies move away from petroleum distillates, liquid fuels based upon other sources (e.g., liquid biofuels) will continue to be important for transportation.

To burn liquid fuels efficiently, it is necessary first to convert the liquid stream into a vapor stream and mix the vapor into surrounding air using a fuel spray. One common approach for steady-flow systems [e.g., low-NOx, lean premixed prevaporized (LPP) combustor ducts for gas turbines] is to inject fuel into a transverse crossflow of air (see e.g., Leong et al. 2000). This process of fuel/air mixture preparation is key to flame stabilization and fuel conversion efficiency. Flames that are stabilized in recirculation zones characteristic of swirl-stabilized LPP combustors, for example, can shift with changes in load. If this causes the local flow field strain rate to exceed the extinction strain rate for the local fuel mixture, the flame will be locally extinguished. This phenomenon degrades combustion efficiency, and localized, transient heat release can also drive thermo-acoustic instabilities, which can ultimately lead to combustor failure. Mixture preparation has a controlling impact on emissions as well. Overly fuel-rich mixing zones can produce large amounts of soot; mixing zones that fall outside the flammability limits are quenched and produce hydrocarbon and CO emissions; while mixing zones near the stoichiometric ratio are very hot, producing high NOx emissions. In many cases, mixture preparation is the most important process for stabilizing and controlling such combustors.

Modern combustor design techniques rely quite heavily upon computational fluid dynamics (CFD). Indeed, CFD has provided advanced designs that significantly improve performance while simultaneously reducing emissions. At present, however, a weak link in every CFD model is the

D. Sedarsky (✉) · M. Paciaroni · E. Berrocal · P. Petterson
Combustion Physics, Lund University, Lund, Sweden
e-mail: david.sedarsky@forbrf.lth.se

J. Zelina · J. Gord
Air Force Research Lab, Wright-Patterson Air Force Base, Dayton, OH, USA

M. Linne
Division of Combustion, Department of Applied Mechanics, Chalmers University, Gothenburg, Sweden

description of the breakup process for the liquid fuel spray, especially the processes that occur immediately after the liquid exits into the gas. The most common numerical approach is to avoid detailed description of primary breakup in favor of an empirically based model describing the sudden appearance of large droplets with specific momentum that then breakup into finer droplets and vaporize (the so-called "blob" model, see e.g., Reitz and Rutland 1995). The code thus relies upon experimental data from existing fuel injection hardware to calibrate the inlet condition to the simulation; it is not a fully predictive scheme. To further improve design capabilities will require a fully predictive description of the spray breakup process. Further out, one could imagine scenarios where advanced modeling of fuel spray breakup would lead to active or passive control of the spray itself, providing optimized performance over the entire turndown range.

The goal of the work described here is to further the development of models by providing detailed observations and statistics on the process of liquid column breakup, for use as a model development and validation database. Not all of the existing data can be presented in this paper, so we provide an introduction to the database. This is a first installment in the database; more is required to develop a full description but sufficient work has been completed to introduce it.

2 Background

A liquid jet issuing into a crossflow of air undergoes a sequence of processes that cause it to break into drops which then vaporize. The process by which a contiguous column of liquid initially breaks into drops is typically called "primary breakup". The drops formed during primary breakup ("primary droplets") can then undergo "secondary breakup" into smaller droplets which ultimately evaporate and form the desired cloud of vapor. The diagram in Fig. 1 depicts a number of breakup mechanisms

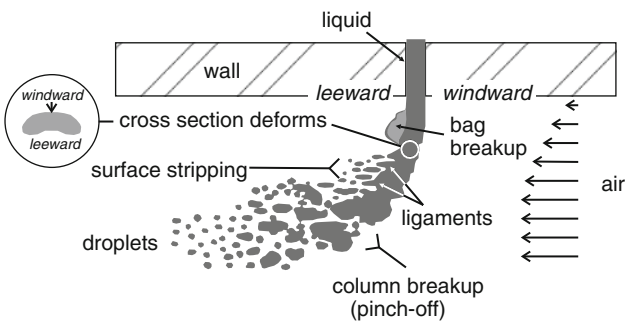

Fig. 1 Schematic of a liquid jet issuing into a crossflow of air. The image is somewhat artificial as all of these breakup processes are not usually observed at the same time

in one schematic. In the discussion that follows, we assume that the cylindrical liquid column that issues from the wall of the channel into the air is not highly turbulent (e.g., turbulent primary breakup does not occur) and it does not experience cavitation within the liquid. In short, without the crossflow it would simply form a vertical, cylindrical column of liquid unperturbed by anything but gravity and small rates of shear at the liquid/gas interface. The crossflow of air, however, causes the column to bend downwind due to the pressure difference that is established across the column. In cross-section, the deformation of the column appears kidney-bean shaped, as a result of a counter-rotating vortex pair (CVP) formed in the liquid by aerodynamic shear. The windward side of the column establishes a stagnation zone in the oncoming air stream, while the leeward side establishes a low-pressure wake. This pressure imbalance generates the structural changes in the column because the liquid is readily deformed. Moreover, if gas with momentum is entrained in the liquid column, downwind-directed momentum exchange to the jet can occur. This happens more readily when a gas jet issues into a gaseous crossflow, but it can also contribute to the jet trajectory of a liquid issuing into a gaseous crossflow.

The penetration of the liquid jet into the gas is controlled somewhat by the ratio (q) of jet momentum flux to gas momentum flux, given by:

$$q \equiv \rho_j U_j^2 / \rho_g U_g^2 \tag{1}$$

where subscript j denotes the liquid jet and subscript g denotes the gaseous crossflow. Clearly, when the jet has significantly more relative momentum than the gas, it will penetrate deeply into the gas flow, and when the jet has very low relative momentum, it will be swept along in the boundary layer of the gas flow.

Primary breakup can occur via a number of processes, and real jets in crossflow tend to break up under a combination of them (often called "mixed mode breakup"). First, longitudinal waves are induced by the gas flow along the windward side of the column, and when their wavelength is larger than the jet diameter, the amplitude of these waves grows in the downstream direction of the liquid, similar to the Rayleigh–Taylor instability of a dripping stream. Ultimately, the column can break at a wave trough ("pinch-off"), producing a very large drop or "blob", in the nomenclature of the Reitz model (Reitz and Rutland 1995). This pinch-off process is also called "column breakup". At the same time, the gas flowing past the stagnation point on the liquid column accelerates as it flows around to the sides of the column. This flow can develop transverse surface waves. At moderate relative gas velocities, these waves can form extended membranes that stretch downstream of the column, often inducing what is termed "bag breakup". This name is adapted from a

process that occurs during droplet breakup. Here, the air pressure spreads a droplet into a thin membrane which then disintegrates into small droplets. As the droplet expands before disintegration, it looks like a small, transparent bag (or perhaps like a miniature jellyfish).

Disintegration occurs because the surface forces exceed the surface tension holding the bag together. For a jet in crossflow, similar bag structures can appear downstream of the column and they disintegrate in similar ways, producing small primary droplets. During this process, longitudinal surface waves on the windward side of the column can still be observed. As the gas speed is increased, however, the wavelength decreases to less than the jet diameter (undergoing a transition to Kelvin–Helmholtz instability); this can also generate pinch-off of sorts, but of smaller structures with smaller primary drops. As the air speed increases further, the rate of membrane formation and disintegration increases until the membranes themselves can not be sustained. At this point, streamers that appear to originate from the crests of longitudinal waves are stripped along the column surface and ejected more energetically from the side of the column as ligaments and droplets. This process is termed "surface stripping" or sometimes "aerodynamic stripping". Under some conditions, longitudinal waves are not observed on the windward side, but they are observed to develop toward the leeward side under surface stripping. These are typically called "leeward waves". Note that both bag breakup and surface stripping commonly fall under the rubric "shear breakup".

A number of fluid processes and properties control primary breakup. One process can dominate over the others within certain flow regimes; regimes that are roughly delineated by two non-dimensional numbers. The Weber number (We) is defined as a ratio between forces that act to break apart a liquid structure and the surface tension acting to hold it together. For each style of spray, We is defined in a particular way that most appropriately emphasizes the critical breakup processes. For a jet in crossflow, We is typically defined in terms of the gas velocity and the jet diameter by:

$$We \equiv \frac{\rho_g U_g^2 d_j}{\sigma_j} \tag{2}$$

where ρ_g is the gas density, U_g is the gas velocity, d_j is the jet diameter, and σ_j is the jet (liquid) surface tension. Typically, regime maps are created showing boundaries between various breakup regimes as a function of We. When viscosity is relatively high, it can affect the boundaries and this effect is cataloged in terms of the Ohnesorge number:

$$Oh \equiv \frac{\mu_j}{\rho_j d_j \sigma_j} \tag{3}$$

where μ_j is the liquid viscosity and ρ_j is the liquid density. In this work, we have performed experiments at low Oh and so viscosity does not have a significant impact. In this regime, column breakup dominates when We is low and shear breakup dominates at high We.

A dynamic phenomenon that is sometimes mentioned in the literature is a periodic unsteadiness in the overall jet. The few reports that discuss this subject assert that it is caused by unsteady shedding of large-scale, cross-flow structures from the liquid column (Ragucci and Cavaliere 2007; Salewski 2006; Salewski et al. 2008). This unsteadiness does not affect primary breakup significantly, but it does affect the jet trajectory. Unsteady phenomena are difficult to present in a journal article, which may explain why it is not routinely discussed.

Jets in crossflow have been studied by a number of groups (see e.g., recent reviews by Leong et al. 2000; Salewski 2006). Experimental work has focused primarily upon characterization of breakup regimes, jet trajectory, jet breakup length and/or time, and measurement of droplet size distribution and density. The work described here emphasizes primary breakup and jet trajectory.

Roughly 10 years ago, Wu et al. (1997, 1998) reviewed prior work and described new results for a liquid fuel jet in crossflow. Their nozzle design was similar to the one used here, including a gradual taper to the exit diameter, but their flow conditions were somewhat different (they examined higher Weber numbers; $71 < We < 594$ and smaller jet Reynolds numbers; $3.4 \times 10^3 < Re < 10.4 \times 10^3$). The main diagnostic tool used by Wu et al. was pulsed shadowgraphy (using a frequency doubled Nd:YAG laser). They studied a sequence of flows where one of the controlling parameters was varied and the others held constant. For example, they varied We by changing d_j while holding q constant, which required them to change U_g as well. This raises the point that some of these parameters can interact with each other. Wu et al. present a breakup regime map plotting q on the ordinate and We on the abscissa. Their map produces recognizable breakup regime boundaries in terms of We. For $We < 11$, the jet broke up via column breakup. At somewhat higher We ($11 < We < 30$), a transition occurred where both column and bag breakup were observed. At $30 < We < 90$, breakup was a multimode phenomenon with bag breakup giving way to surface stripping, and for $90 < We$, they report surface stripping alone. Wu et al. also show a dependence upon q. Most of the rest of their paper focuses on correlations for column trajectories.

More recently, Faeth et al. (Mazallon et al. 1999) and Sallam et al. (2004) reported on studies of similar jets. Their injector design had a small plenum with a sudden, sharp-edged orifice ("Borda" and "supercavitating" nozzles, see Mazallon et al. 1999) which are different from the

gradually tapered inlet described by Wu et al. Both a shock tube and a subsonic wind tunnel were used to provide the crossflow in this work. The flow conditions used by Faeth et al. were roughly the same as Wu et al. except that they emphasized somewhat lower *We* ($0.5 < We < 250$). Faeth et al. used pulsed shadowgraphy (using a frequency doubled Nd:YAG laser) to observe the column and jet structure, and pulsed holography (using a similar laser) to measure the droplet distributions throughout the jet. These authors produced a breakup regime map and in fact compared the results from their first set of experiments (Mazallon et al. 1999) to their second set (Sallam et al. 2004). They found that for *We* less than 4–5, the jet broke up selectively via column breakup. At somewhat higher *We* (30–60), a transition occurred where both column and bag breakup were observed. At *We* around 110, breakup was a multimode phenomenon with bag breakup giving way to surface stripping. These results are fairly similar to those of Wu et al. Contrary to Wu et al., however, Faeth et al. reported that breakup regimes are not affected by q. Sallam et al. assert that increased liquid stream velocity simply stretches out the jet trajectory and produces higher speed droplets, nothing more. Because q scales with velocity squared but *We* scales with velocity, there may be subtle effects associated with various experimental approaches that are not captured by most regime maps. Sallam et al. also infer the wavelength ("λ_s") of the longitudinal waves on the windward side (as we do here), discuss how they change with conditions, and then report correlations between λ_s/d_j and breakup. When $\lambda_s/d_j > 1$ column breakup was observed, when $\lambda_s/d_j \approx 1$ bag breakup was observed, and when $0.1 < \lambda_s/d_j < 1.0$ a multimode region featuring surface stripping and column breakup was observed. This is really just a restatement of the way that wave structure changes with *We*, and in fact Sallam et al. provide this correlation:

$$\lambda_s/d_j = 3.4We^{-0.45} \tag{4}$$

Faeth et al. then develop correlations for column trajectories.

Other groups have also studied liquid jets in crossflow experimentally but with somewhat less emphasis on the primary breakup process. Bellofiore et al. (2008) and Cavaliere et al. (2003) have recently emphasized the entire flow field for jets issuing into high-pressure airflows (1–4 MPa). They observed these flows using pulsed laser shadowgraphy and PIV, acquiring a number of images and performing careful image analysis to extract information on trajectories, for example. Researchers at the DLR in Cologne (Freitag and Hassa 2008; Rachner et al. 2002) have performed similar elevated pressure studies on aircraft fuels, applying white light shadowgraphy and phase doppler anemometry to obtain droplet size distributions and velocity information in the dispersed (downstream) region of the flow. They present jet trajectories; droplet size distributions, locations and volume flux; and gas velocity and turbulent energy. Their shadowgrams show that realistic sprays like these are highly atomizing (and optically dense), and their images contain evidence of the overall jet unsteadiness mentioned earlier. Other related work (including computation and theory) is discussed in the reviews presented by Leong et al. (2000) and by Salewski (2006), and the references cited in those reports.

In this paper, we report initial imaging studies aimed at development of a comprehensive database on the breakup of liquid jets in crossflow. Unfortunately, no single diagnostic technique can provide all of the information required to describe the entire spray breakup problem. Flow field dynamics can be captured via particle image velocimetry, laser Doppler velocimetry, and/or phase Doppler anemometry. Shadowgrams of the entire spray also prove useful, and when used with a fast framing camera, one can observe unsteady processes. A number of commercially available droplet-sizing techniques are discussed by Bachalo (2000), but they typically work only in dilute regions of a spray. Laser light scattering and extinction can also be used for droplet sizing, and when performed in the infrared, this technique can be used in fairly dense sprays (Parker et al. 1998). Planar imaging of elastic scattering (Mie and Rayleigh) can sometimes be used to differentiate vapor from liquid mass, or as an alternative Exciplex imaging is a way to use laser- induced fluorescence to differentiate vapor from liquid (but it requires the absence of oxygen for quantitative determination). A technique called "laser sheet dropsizing", or alternatively "planar laser dropsizing" (Greenhaulgh and Jermy 2002), relies upon a ratio between the laser-induced fluorescence image of droplets and the Mie scattered image of the same droplets. In principle, LIF scales as the droplet diameter cubed (volumetric) while Mie scattering scales as the diameter of the droplet squared (surface). A ratio of the two images, properly scaled, can thus provide an image of droplet sizes in relatively dilute sprays (with uncertainties, see e.g., Berrocal 2006). Planar imaging techniques are plagued by multiple scattering from droplets (which changes as a function of position in the image) but a new technique called structured laser illumination planar imaging (Berrocal et al. 2008) promises to mitigate many of these effects.

While there are many reports covering very good work on sprays, the region that has proven very difficult to explore is the interior of a highly atomizing spray. Dynamics in this region often control the initial droplet distribution, but the fog of surrounding droplets can sometimes be so dense that normal measurement techniques are

unable to penetrate. In this study, the aim was to begin to provide comprehensive experimental observations of jet in crossflow breakup processes under a wide range of conditions, including optically thick conditions that were previously considered too dense for optical diagnostics. The data are intended to be used as a validation database that will be available to interested users; to be expanded and updated as new experiments are conducted.

3 Experimental systems

3.1 Jet in crossflow test section

The test section used in this work was designed in close collaboration with a group of large eddy simulation (LES) developers at Lund University (Salewski 2006), specifically for detailed observation of a variety of jet-in-crossflow conditions. Requirements included the need for the largest practical length-to-width ratio (to develop the flow as much as possible), minimum turbulence in both the emergent spray and the channel air flow, the ability to make measurements in the near-field and wake regions while simultaneously observing the overall jet and downstream region, and the ability to achieve representative values for We and q.

The test channel design (see Fig. 2) consists of a square channel constructed of aluminum profile measuring 3.1 m in length with 80 mm sides (internal dimensions). The test section containing the spray incorporates five optical glass windows that are mounted flush with the inside wall. On the top of the channel, where the nozzle is located, two 50 mm square windows are located directly upstream and directly downstream of the nozzle. There are 80 mm × 100 mm windows along both sides of the test section, and they sit flush with the top of the channel and the spray outlet. The window along the center of the bottom is 20 mm × 100 mm. This configuration allows complete optical access to the spray.

The crossflow of air is provided by a 4 kW centrifugal fan with a maximum static pressure of 4.2 kPa, resulting in a maximum air speed of 74 m/s. The fan outlet is connected to the test channel via flexible tubing. Aluminum mesh screening is positioned at both ends of the flexible tubing to render the flow more uniform across the pressure drop of the screen. A short section of honeycomb is mounted at the entrance to the straight test section channel in order to reduce any swirl or large-scale turbulence induced by the fan and the tubing.

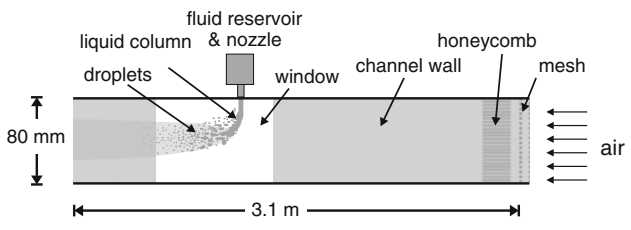

Fig. 2 Schematic of the flow channel used in this work

The pressurized liquid nozzle design consists of four interchangeable nozzle tips of varying exit diameters: 0.5, 0.7, 1, and 1.25 mm. These nozzles are replicas of the atomizer nozzles in use at the University of California at Irvine Combustion Laboratory, and a schematic is shown in Fig. 3. The taper allows the flow to accelerate without inducing further unsteadiness or cavitation. In addition, this design simplifies modeling if the interior flow is to be included in models. The nozzles are threaded into a small fluid accumulator chamber, held in place over the test section with the nozzle exit flush with the channel walls. The fluid accumulator base diameter is 62 mm which is 50 times the largest nozzle orifice diameter. The fluid chamber is filled via a 5 l reservoir which is pressurized appropriately to provide the flow velocity as specified in Table 1. The accumulator chamber is filled completely prior to

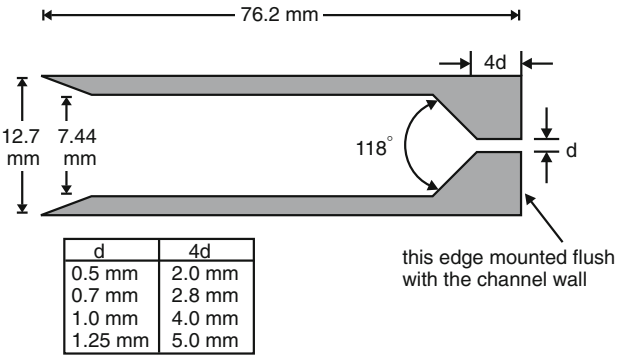

d	4d
0.5 mm	2.0 mm
0.7 mm	2.8 mm
1.0 mm	4.0 mm
1.25 mm	5.0 mm

Fig. 3 Schematic of the nozzle design used in this work

Table 1 Jet-in-crossflow run conditions

We	Case	d_j (mm)	U_j (m/s)	U_g (m/s)	Re_j	q
21	9	0.5	10.4	48	5.18×10^6	37
21	2	0.5	21	48	1.05×10^7	153
29	4	0.7	21	48	1.46×10^7	153
34	8	0.5	13.5	62	6.72×10^6	38
40	7	0.5	15	67	7.47×10^6	40
41	6	1	21	48	2.09×10^7	153
49	1	0.5	21	74	1.05×10^7	64
68	3	0.7	21	74	1.46×10^7	64
98	5	1	21	74	2.09×10^7	64
122	10	1.25	21	74	2.61×10^7	64

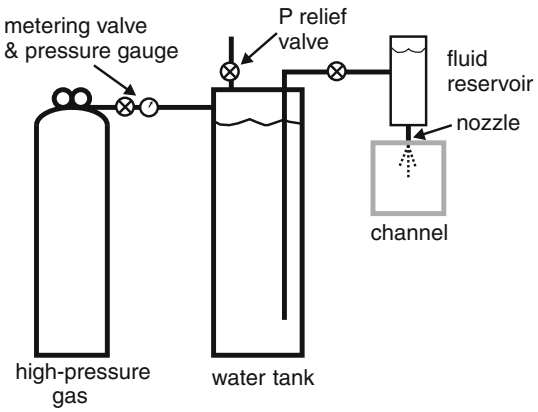

Fig. 4 Schematic of the pressure accumulator system

commencement of the measurement. A schematic of the pressure accumulator system is detailed in Fig. 4.

3.2 Jet-in-crossflow conditions

This study covers ten test conditions with varying Weber numbers and momentum flux ratios. These conditions were chosen to cover a range of conditions examined in previous literature within the operating range of the test section while using pure water (Chen et al. 1993; Madabhushi 2003; Madabhushi et al. 2004; Rachner et al. 2002; Salewski 2006; Wu et al. 1997, 1998). The full set of test conditions is shown in Table 1.

The data presented here were acquired using four orifice diameters; the first six test conditions cover the three smallest orifice diameters at both a maximum Weber number and a moderate Weber number. Test conditions seven through nine include various combinations of air velocity and jet velocity while holding the momentum flux ratio nearly constant. Test condition ten utilized the largest jet orifice diameter in conjunction with the maximum air speed resulting in a maximum Weber number of 122 for this set of water experiments.

Case numbers referring to specific experimental conditions are included in the tables provided here and referenced directly in the discussion to facilitate access to the data for further exploration. While this is a convenient way to organize the database, the flow regimes follow a different pattern. Hence, the tables and analysis presented in the following paragraphs are arranged in order of ascending Weber number to enable a coherent discussion of breakup in this spray.

3.3 Imaging diagnostics used in this study

Three imaging techniques were used in this study; including particle imaging velocimetry (PIV), high-speed shadowgraphy (HSS), and ballistic imaging (BI). These diagnostics were selected to provide relevant experimental information and, where possible, to avoid or mitigate the multiple scattering effects that frustrate most imaging measurements in dense spray regions. The imaging work presented here does not provide a fully comprehensive validation database, but it does represent a significant collection of useful information that can provide insights and initiate comparisons with models.

3.3.1 Particle imaging velocimetry

Particle image velocimetry (PIV) is a commercially available laser diagnostic used here primarily to characterize the gas-phase crossflow. For these measurements, the crossflow air was seeded upstream of the test rig with dry 0.5 μm $ZrSO_4$ particles via a LaVision cyclone seeder using magnetic stirring. The beams from two frequency doubled Nd:YAG lasers (Quantel) were overlapped and expanded into a sheet to generate successive Mie scattering from both seed particles in the air stream and the spray itself. The laser sheet was aligned along center of the test section, with sheet thickness of 700 μm. The energy in each pulse was set to approximately 30 mJ, and the pulse separation was optimized for each case investigated. An interline-transfer CCD camera (PCO, 1,024 × 1,248 pixels) was aligned normal to the air flow direction and focused onto the light sheet to capture the PIV images.

In order to create a two-dimensional map of the spray region, horizontal and vertical cross sections passing through the centerline of the nozzle were investigated. The glass windows in the test section allowed for only partial imaging of the 86 mm cross section, however. Reflections from the walls of the test rig presented difficulties in some regions of the PIV images, despite the use of an interference filter at the camera to suppress background light.

Flow velocities were calculated from the PIV images using a cross-correlation algorithm with an adaptive multipass method developed by LaVision. Each image from the CCD camera has 1,024 × 1,248 pixels, which are divided into 32 × 32 pixel interrogation regions for cross-correlation. To generate velocity profiles (average and rms values) of the flow through the channel, the data from 60 PIV recordings were used.

A few PIV images were also collected with the spray turned on. However, it is important to point out that the correlation algorithm is sensitive to the intensity of the image pixels. In the spray region, larger drops will scatter more light, causing them to register a higher intensity in the image. In some cases, this can lead to a bias error, when similar densities of small and large particles are correlated. The PIV images with the spray turned on are therefore used only to visualize the spray and its influence on the flow field.

3.3.2 High-speed shadowgraphy

High-speed shadowgraphy (HSS) is a line-of-sight measurement where a high-intensity light source is used to illuminate the object of interest (the spray in this case). A high-speed imaging detector is positioned opposite the light source and used to record the shadow cast by the object. In the work reported here, one window of the channel was covered with a translucent screen and illuminated with an array of bright white-light LEDs. A Phantom 7.0 high-speed camera from Vision Research, capable of frame rates up to 4,800 frames/s, was placed on the opposite side and it recorded a series of high- speed videos for each of the ten test conditions. This imaging method can reveal non-uniformities in the spray and is useful for determination of the liquid/gas interface, approximate spray breakup length, cone angle, and penetration length. In addition, high-speed imaging allows one to observe unsteadiness in the jet flow field. The price one pays is that high-speed cameras have somewhat limited spatial resolution. Spatial resolution can also be limited, however, in optically dense regions due to noise from multiply-scattered light (Dunsby and French 2003).

3.3.3 Ballistic imaging

Ballistic Imaging is a line-of-sight imaging technique that generates high-resolution shadowgrams or schlieren-type images of structures buried inside turbid media by mitigating signal noise caused by multiply-scattered light. It can thus be applied to generate high-resolution images through materials that appear opaque to conventional imaging techniques. The development and evaluation of a single-shot, time-gated ballistic imaging instrument for use in spray research have been described in detail by Paciaroni (2004) and by Paciaroni and Linne (2004). This diagnostic has been used to observe primary breakup in a steady atomizing water spray (Paciaroni et al. 2006), a transient diesel spray (Linne et al. 2006), and a series of sprays in crossflow (Linne et al. 2005). The technique has recently been reviewed by Linne et al. (2009). The high-resolution, single-shot images generated by a ballistic imaging system allow the observation of small-scale and near-field spray structures such as droplets, voids, and ligaments under dense spray conditions. Since it is a fairly new technique, we describe it in somewhat more detail here. Readers interested in the full details should consult Paciaroni and Linne (2004) and Linne et al. (2009).

The ballistic imaging instrument used in these experiments is depicted in Fig. 5. Ballistic imaging gets its name from the fact that a small class of photons (commonly termed "ballistic photons") can be transmitted through highly turbid media without scattering. They can thus be

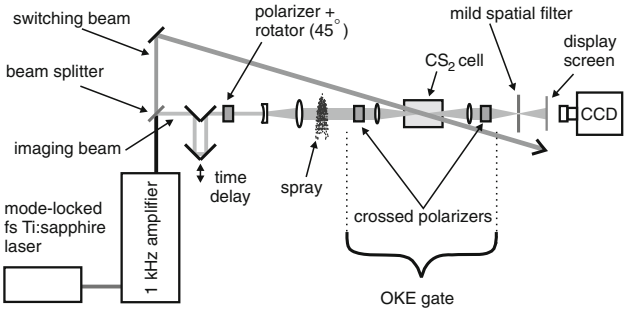

Fig. 5 Schematic of the ballistic imaging instrument used in this work

used to create an image of large structures buried inside the turbid medium (e.g., a liquid column buried inside a dense fog of droplets). To do this requires one to isolate high-quality imaging light from all of the other background and noise photons, and then to construct the image using just the selected class of photons. That is done here mostly by taking advantage of the fact that high-quality imaging photons are first to exit (we use an appropriately triggered, very fast shutter) and maintain the original polarization of the input light (we filter out background light using polarizers). Careful design of the optical system also contributes.

A 1-kHz repetition rate Spectra Physics Spitfire Ti:Sapphire regenerative amplifier, seeded with a Spectra-Physics Tsunami Ti:Sapphire mode-locked laser was used to generate 1 mJ pulses with a pulse duration of 80 fs, centered in wavelength at 800 nm. The linearly polarized beam exiting the amplifier was split into an optical kerr effect (OKE) switching beam and an imaging beam. The OKE gate serves as a 2 ps shutter that is triggered by the switching pulses. The imaging beam was time delayed using an adjustable length delay arm, allowing control of the temporal overlap between the switching and imaging pulses at the OKE gate. The linear polarization of the imaging beam was ensured before the light could enter the spray using a polarizer. The polarization of the beam was then rotated 45° to provide the appropriate polarization state for the OKE polarization switching. The imaging beam then passed through a telescope used to control the size of that beam as it crosses the spray, relay optics which focus the beam through the OKE switch, and a final telescope for imaging to a display screen. The image was recorded by an iXon DU-897 CCD camera with on-chip gain made by Andor.

Until recently, the simplest explanation of ballistic imaging has been to state that a ballistic image is simply a specialized shadowgram, and to first order this explanation has sufficed. There are, however, some subtle but important differences between a shadowgram and a schlieren image. As Settles (2001) points out:

Most of the drawbacks from shadowgraphy stem from its essential ambiguity *A shadowgram is not an image; it is a shadow*. There is no 1:1 correspondence between the object and its shadow (as there is between an object and an image in schlieren optics, where a lens generates an optically conjugate relationship between the two). Thus, shadowgrams are not true-to-scale in general. Only the dark regions of a shadowgram can yield an undistorted representation of the schlieren object, since they mark where the deflected rays originate. The bright zones mark where the rays end up, which is potentially misleading. Light rays can overlap, cross, and intersect before forming a shadowgram if the screen distance is large enough, thus forming *caustics*.

Note that classical schlieren imaging uses spatial filtering to remove noise and fundamentally change the signal from a flow field image lacking high scattering orders. Here, we use time gating to remove noise and change the image collected from flow fields with high scattering orders. In both cases, a lens generates an optically conjugate relationship between the object and image. In these respects, it may be more accurate to describe ballistic imaging as a specialized form of schlieren, not shadowgraphy. Until now, it has not been an important distinction.

As discussed by Linne et al. (2009), some sprays are much more turbid (have a higher optical depth, *OD*) than others. Typically, the *OD* scales with *We*; highly atomizing sprays usually have the highest optical depth (this trend is modulated somewhat by the droplet size distribution). The BI instrument described here was originally designed to interrogate atomizing diesel sprays (Linne et al. 2006), which have the highest *OD* and are the most challenging of sprays. Under most conditions, jets in crossflow have a fairly mild *OD*. Especially at low *We*, a well-designed shadowgraph system using mild spatial filtering or perhaps combined spatial and polarization filtering (Linne et al. 2009) could image structures embedded inside the spray. The OKE gated BI system used here then seems unnecessary. Going back to Settles, however, if we wish to image fine details of voids as well as liquid columns, especially voids in the wake region that are related to bag breakup and stripping of ligands, we do wish to image those small open regions unambiguously. The ballistic imaging system will do that for every spray of interest. Moreover, some of the high *We* sprays studied here do have higher *OD* starting about 10 mm past the nozzle. It is also our plan to study jets at higher *We* (using other fluids), and these will indeed require some form of ballistic imaging. In order to present a sequence of results using identical instrumentation with best possible resolution, therefore, we have studied even fairly transmissive sprays with this BI instrument.

3.4 Image analysis

A large number of instantaneous (single-shot) measurements are necessary to provide statistically significant data for the determination of trends. For the case of spray imaging in general, and ballistic imaging specifically, this situation necessitates the use of automated image analysis software tools. Image analysis for the measurements presented here was carried out using a software tool named Xflow, which is based on MatLab image processing routines. This software was developed by the authors specifically for ballistic images and it can also be obtained by contacting the authors. The analysis for jet-in-crossflow images using Xflow relies on threshold and connectivity segmentation of image regions and focuses on five interrelated image features: the main jet, resolved drops, resolved voids, periodic structure appearing on the upstream jet profile, and a droplet distribution determined by fitting droplet data extracted from the images. It is necessary to point out, however, that ballistic imaging is not a formal droplet sizing technique, as droplets that are smaller than the spatial resolution of the instrument will not be included in the analysis. Some sprays (e.g., typical jets in crossflow) produce primary droplets that are well above the spatial resolution cutoff, however, making it possible for image analysis to provide sizing of primary drops in the near-field of the spray.

The main jet is defined as the largest connected object in the image, as such this feature encompasses the jet and any attached ligaments. In the data set images, the direction of liquid propagation is from the top of the image downward, and the direction of the crossflow is from right to left.

Drops are defined as liquid regions appearing in the image distinct from the main jet. Drops are assumed to be spherical for determination of drop diameters, and drop-like features with diameters smaller than the resolution limit of the imaging optics are excluded from this feature set.

Voids are low-signal regions appearing within the main jet or within large drops. Voids are also assumed to be spherical for determining void diameters, and void-like features below the resolution limit are likewise excluded from the analysis.

Periodic structure is defined here as variation from an exponential-fit baseline, calculated along the windward jet profile for jets in crossflow. The peaks of this "variation curve" indicate longitudinal waves on the windward face of the jet. This potentially allows frequency analysis of the variation curve to be related to models and theoretical predictions for gas–liquid shear layer instabilities.

Further characterization of the spray breakup conditions and primary drop sizes can be accomplished by fitting the drop size information extracted from many images to a suitable distribution, such as the modified Rosin-Rammler

distribution. Care should be taken to ensure the images for this analysis are of high quality, adequately represent the spray under observation, and are generated under the same run conditions to ensure an accurate determination of the representative drop distribution.

Threshold and connectivity segmentation is an appropriate choice for separating structures in ballistic images, due to the nature of the jet-in-crossflow spatial features. However, the choice of threshold level can be a point of concern. High-quality images with good signal-to-noise levels are, to some degree, insensitive to changes in detection threshold. In contrast, images with significant noise can be sensitive to small changes in threshold, leading to large uncertainties in the segmentation results. To address this concern, the threshold level used in this work is a dynamic parameter calculated individually for each image, using a method suggested by Otsu (1979). Here, the choice of threshold level is based on an algorithm that minimizes the intraclass variance of the light and dark pixels.

4 Overview of experimental results

The data set associated with this paper consists of PIV images, high- speed shadowgrams, ballistic images, and statistical data extracted from these images for the ten run conditions in Table 1. Here, we present example results and discuss them. Access to the complete data set can be obtained over the internet (contact the authors for instructions).

4.1 PIV

As discussed earlier, PIV was used to characterize the channel flow and demonstrate fairly uniform air flow profiles for all cases studied. PIV images provide no evidence of large-scale or coherent motion. Averaged velocity profiles for the various run cases detailed in Table 1 are presented in Figs. 6 and 7 to serve as a known inlet condition for model development and validation. Note that the profiles in the vertical direction in Fig. 7 are somewhat asymmetric. The reason for this is believed to be either a small flow disturbance caused by the interface at the most upstream window or the presence of the nozzle (both at the top wall). Pitot tube measurements further upstream (upstream of the windows and nozzle) indicated a symmetric profile. Furthermore, the turbulence intensity (U_{rms}/U_{max}, extracted from PIV data) is about 5% in the core flow, but it increases to about 10% close to the wall where the nozzle is located, confirming further this conclusion about the asymmetry. While this asymmetry is not optimum, the profiles were highly repeatable. Our goal in this first publication is to provide initial data so that theoreticians can exercise their models against the data set and offer opinions on the choice of flows, nozzle design, fluid properties, and so forth. Once those issues are settled, we will focus further on this asymmetry of the gas flow with the goal to minimize it and then to characterize fully what remains.

Figure 8 contains an example average PIV image containing both the gas flow and the jet. It depicts a horizontal cut through the flow with the camera viewing it from the bottom window of the channel. The image shows how the spray continuously spreads from the injection point in the cross flow.

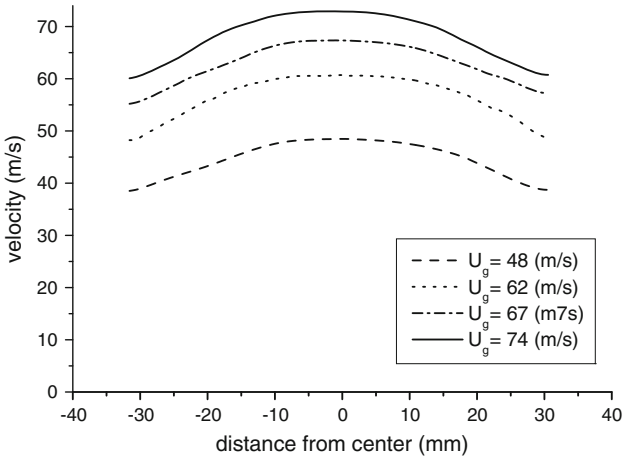

Fig. 6 PIV data for the various gas flow speeds across the channel in a horizontal plane, through the channel centerline at the axial location of the nozzle

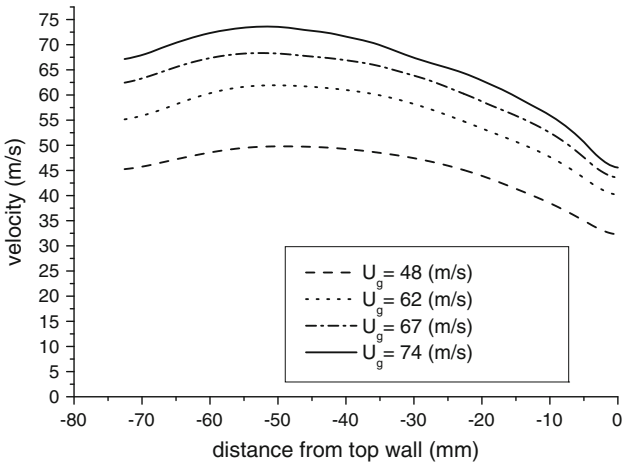

Fig. 7 PIV data for the various gas flow speeds across the channel in a vertical plane, through the channel centerline at the axial location of the nozzle. The top wall (location of the nozzle) is at distance = 0. We attribute the asymmetry in the profile to small irregularities in the top wall (see text)

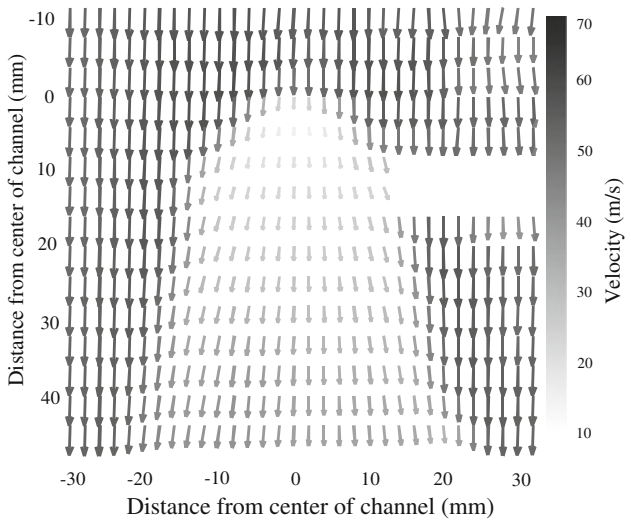

Fig. 8 Average spray pattern (100 images), together with gas and spray velocity captured via PIV in the horizontal plane (case 7, $U_g = 67$ m/s). The laser sheet cut trough the center of the channel in the horizontal direction. Owing to high noise levels, a portion of the velocity vectors in the shadow of the spray column have been removed

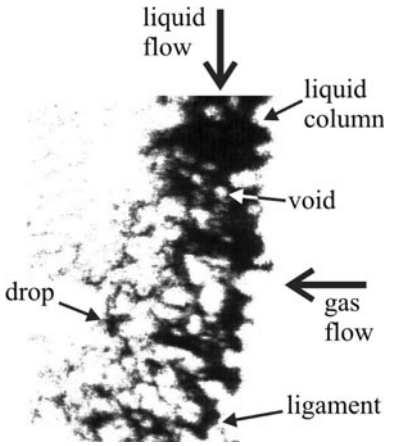

Fig. 9 Example of a ballistic image acquired as part of this work

4.2 Flowfield images

Representative ballistic and high-speed shadowgram images for all of the ten initial test cases are examined and discussed in this section. The inlet nozzle of the spray is located at the top of the images, and the crossflow is from the right hand side to the left. Note that both HSS and BI are line-of-sight techniques, collecting image light in similar forward scatter arrangements.

A number of HSS image sequences for each case can be found in the database; still images from these sequences are shown in the HSS figures that follow. Two fields of view are provided: a large field, showing the entire liquid jet profile, and a smaller field, zoomed to show the flow near the nozzle orifice. The vertical dimension in the fields of view are approximately 7 cm for images that are zoomed out (show the entire jet) and 2.5 cm for the images that are zoomed in.

The ballistic images taken in this experimental campaign use a smaller field of view than the shadowgrams (the field of view can be set by adjusting the telescope in Fig. 5). The ballistic images thus have better spatial resolution than the shadowgrams. A large number of ballistic images were acquired, they can be obtained from the database in various formats, and they have been evaluated using the image analysis scheme described in Sect. 3.4 mentioned earlier. An example single image for test case 1 is shown in Fig. 9. The field of view is approximately 5 mm. In the image, one can see dark areas representing a continuous fluid phase and light areas representing the gas phase. In Fig. 9, one can detect longitudinal waves on the windward side, one can see pinch-off underway, certainly one can see entrainment, and small voids are visible in the liquid possibly caused by entrainment. One can see ligaments stretching downwind and primary (non-spherical) droplets stripping away.

In the discussions that follow, we rely upon both classical white-light shadowgrams and ballistic images. Most fluids researchers are familiar with shadowgrams. They depict the effect of refraction on the light passing through the fluid—producing light and dark regions that help one identify thinner and thicker structures and the edges of the liquid/gas interface. Ballistic images are also a form of shadowgraphy or Schlieren. Ballistic images provide additional information because the system recovers a special subset of the total light passing through the fluid structure. This light was not strongly affected by spatial noise, which allows one to image what lies inside a highly scattering field of droplets. Unfortunately, there is normally very little of this high-quality light so a low light level imaging system is used. This results in increased contrast and a lower effective dynamic range, yielding images which appear distinct and flat compared to a white-light shadowgram. One can still achieve fairly high spatial resolution, however (Paciaroni and Linne 2004). The interior of the contiguous liquid structure is not visible in ballistic images mainly because the liquid is thick and it has a non-negligible index of refraction. The light passing through the liquid is thus delayed to the point where much of it can not be transmitted through the OKE gate before it shuts. This happens whenever the liquid is thicker than about 130 μm for a 2 ps shutter and provides the additional benefit suppressing extraneous light (caustics) refracted by liquid surfaces.

The discussion presented here, and the flow cases presented in Table 1 are ordered by ascending Weber number. This choice is based upon the notion that *We* is the

most important non-dimensional number for description of breakup. What we find, however, is that *We* is not the only important determinant of breakup. In the "near field" (very close to where the liquid exits the nozzle into the gas), for example, the liquid stream is controlled much more by the characteristics of the liquid flow and perhaps by the interior of the nozzle, not the gas flow. This early condition for the liquid stream has an effect on the entire jet. The breakup regime maps provided by Wu et al. (1997, 1998) and by Faeth et al. (Mazallon et al. 1999) and Sallam et al. (2004) have a large amount of scatter in the data, probably for the same reasons.

Case 9 has the lowest *We* (21) with the lowest value of q (37) as well. The Reynolds number is 5.2×10^6. Figure 10 includes three shadowgrams of the jet. Figure 10a shows the trajectory of the jet as it breaks up. One can clearly see evidence for classical column breakup as the jet bends, together with some other form of breakup producing smaller primary droplets nearer to the nozzle exit. Figure 10b shows the liquid column just as it exits into the gas and in fact one can see a small bag in formation. In the motion pictures, these bags form and then break repeatedly. Breakup is thus mixed mode with bag and column breakup. Classical Rayleigh–Taylor wave structures are also in evidence in Fig. 10b and these are what grow into the waves that pinch-off. Some 12.7 mm below the nozzle in Fig. 10c, one can see classical column breakup developing at the same time that bag breakup is occurring.

Just as in Fig. 10, the ballistic image in Fig. 11a contains evidence for classical column breakup as the jet bends. The smaller primary droplets visible in the shadowgram (Fig. 10) are not found in the BI because it purposely avoids imaging small features like the droplets. At a position 2 mm below the nozzle, one can also see a small bag forming in the ballistic image. Mixed mode breakup is clearly in evidence and classical Rayleigh–Taylor wave structures are also visible.

Case 2 has the same *We* (21) with a much higher value of q (153) and Reynolds number ($Re = 1.1 \times 10^7$).

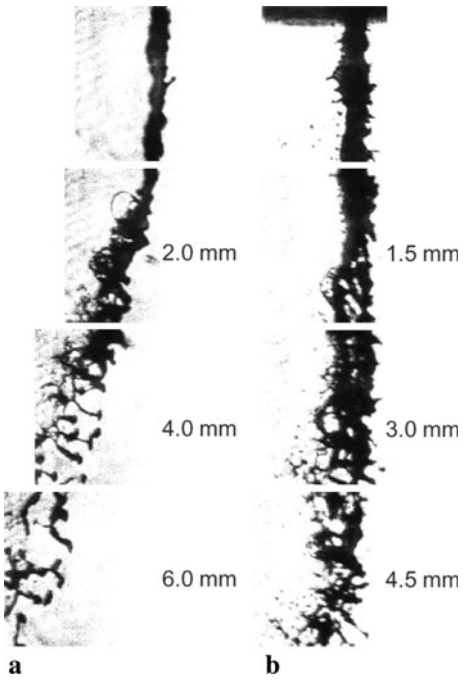

Fig. 11 Ballistic images of **a** case 9 ($We = 21$, $q = 37$, $Re = 5.2 \times 10^6$, $d_j = 0.5$ mm), and **b** case 2 ($We = 21$, $q = 153$, $Re = 1.1 \times 10^7$, $d_j = 0.5$ mm). Numbers provided on the right hand side of each composite image indicate vertical distance the spray system was raised (beam lower in the spray) relative to the position at the nozzle

Figure 12 includes two shadowgrams of the jet. The breakup in this regime is fairly classical mixed mode combining column and bag breakup, although column breakup dominates. Figure 12a shows the trajectory of the jet; one can clearly see that the jet column is pinching-off into large primary drops via column breakup. Figure 12b shows the liquid column just as it exits into the gas. One can see classical Rayleigh–Taylor wave structures, small bag formation downstream, and the onset of column breakup. The main contribution of high q (the difference between Figs. 10, 12) is that the jet penetrates further into the gas but breaks apart in much the same way, consistent

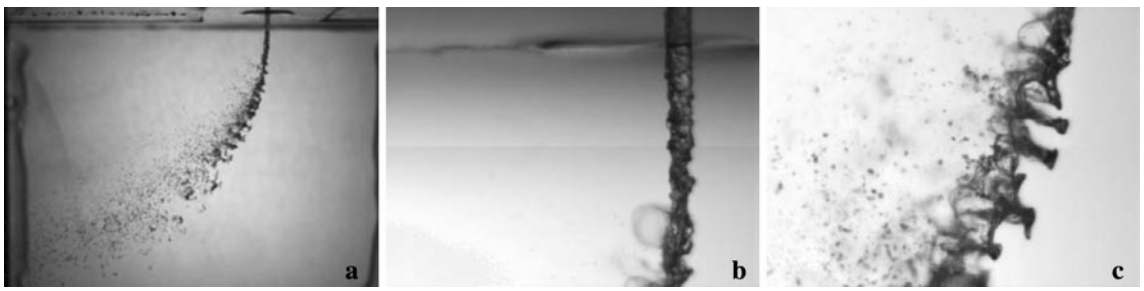

Fig. 10 Shadowgrams of the jet in Case 9 ($We = 21$, $q = 37$, $Re = 5.2 \times 10^6$, $d_j = 0.5$ mm). **a** Zoomed out to see the spray trajectory, **b** zoomed in right at the nozzle exit, and **c** zoomed in but 12.7 mm down from the nozzle exit. Note, in **a** and **b**, a symmetric shadow of the jet is visible above the nozzle orifice in the images; this should not be interpreted as a continuous jet extending to the top of the image

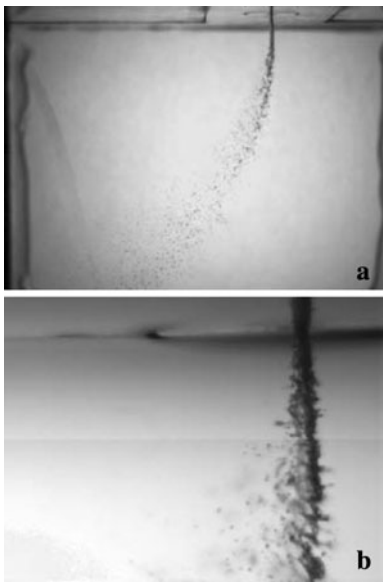

Fig. 12 Shadowgrams of the jet in Case 2 ($We = 21$, $q = 153$, $Re = 1.1 \times 10^7$, $d_j = 0.5$ mm). **a** Zoomed out to see the spray trajectory, **b** zoomed in right at the nozzle exit. Note, a symmetric shadow of the jet is cast above the nozzle orifice in the images; this should not be interpreted as a continuous jet extending to the top of the image

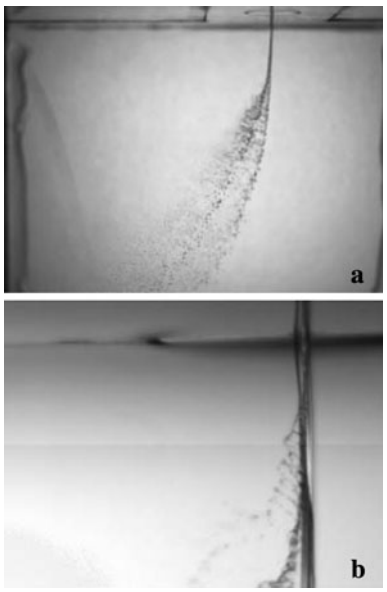

Fig. 13 Shadowgrams of the jet in Case 4 ($We = 29$, $q = 153$, $Re = 1.5 \times 10^7$, $d_j = 0.7$ mm). **a** Zoomed out to see the spray trajectory, **b** zoomed in right at the nozzle exit. Note, a symmetric shadow of the jet is cast above the nozzle orifice in the images; this should not be interpreted as a continuous jet extending to the top of the image

with the assertion of Sallam et al. (2004). This fact is demonstrated more clearly in the ballistic image of this jet (see Fig. 11b). Case 2 also has a Reynolds number twice as large as that of Case 9 and that would explain the higher level of small-scale surface disturbance.

It is important to point out here that the database also contains ballistic images of each case further downstream. These supplementary data are from an imaging position offset from the nozzle centerline by 3 mm downwind. They are not displayed here because they are not easy to collect into a composite image. The ballistic images show breakup at the tip similar to the tip in Figure 11a. As mentioned earlier, the Reynolds number for case 2 is much higher than in case 9, and this explains the difference in small-scale surface disturbances (more obvious in the ballistic images) between the two jets in Fig. 11. Longitudinal waves are clearly seen on the windward surfaces of both images.

The two cases discussed so far (9 and 2) use a nozzle with diameter of 0.5 mm, while the next case in the *We* sequence (case 4 with $We = 29$, $q = 153$, $Re = 1.5 \times 10^7$) steps up one nozzle size to 0.7 mm. Figure 13 includes two shadowgrams from case 4. While the jet trajectory image (Fig. 13a) shows some evidence of column breakup like other jets discussed so far, what is more interesting is the formation of multiple, distinct streamers each of which break up via some form of pinch-off. The trajectory images suggest some form of bifurcation (Reynolds et al. 2003). One can also detect the same phenomenon in the only other case that uses this 0.7 mm diameter nozzle (case number 3 shown in Fig. 14). We present case 3 ($We = 68$, $q = 64$ and $Re = 1.5 \times 10^7$) here as well, although that is out of the *We* sequence, because this is a fairly unusual and

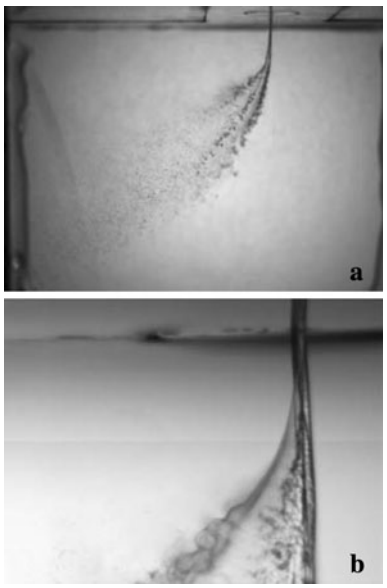

Fig. 14 Shadowgrams of the jet in Case 3 ($We = 68$, $q = 64$, $Re = 1.5 \times 10^7$, $d_j = 0.7$ mm). **a** Zoomed out to see the spray trajectory, **b** zoomed in right at the nozzle exit. Note, a symmetric shadow of the jet is cast above the nozzle orifice in the images; this should not be interpreted as a continuous jet extending to the top of the image

distinct phenomenon. Inspection of the nozzle itself via optical microscopy shows no structural difference in this nozzle when compared to the others (e.g., no internal scoring or unusual ellipticity to the exit), other than the differences in diameter. While some of the other cases show some evidence for this kind of behavior, these are the two jets that show it distinctly, and it is related to this particular nozzle and perhaps the liquid flow speed (it was the same for both cases). Figure 13b shows the jet near the nozzle exit. There one can see that the crossflow strips a thin membrane off of the column and sweeps it downstream, and the membrane shows clear evidence of vorticity in the fluid that forms it. The main difference between cases 4 (Fig. 13) and 3 (Fig. 14) is that the air speed was increased for case 3 and that increased the value for *We* while decreasing q. This difference in air speed caused the membranes to strip more readily from the column in case 3. Here, one finds even more clearly that the crossflow strips a thin membrane with residual vorticity off of the column and sweeps it downstream. Note also that windward, longitudinal surface waves do not develop near the nozzle in this jet and this is perhaps the reason that contiguous membranes are more easily formed (versus smaller scale "bags") than in the other cases. Classical bifurcation involves an induction via interacting vortices (e.g., the counter-rotating vortex pair, CVP, in the liquid column). The images in Figs. 13 and 14 do not conclusively demonstrate this behavior, and so the further work will be required to determine whether or not this jet is bifurcating in the classical sense. All the same, to have a jet in crossflow rapidly form additional streamers with significant mass is a promising phenomenon from a practical viewpoint where rapid breakup and broad distribution of fuel are desired.

The ballistic images show the membranes stripping from the surface just as the shadowgrams do, but the ballistic images also show that there are more than just two vertical streamers coming off the column. Because the far field shows just two of them, these extra streamers probably coalesce into a total of two just downstream (Fig. 15).

Case 8 is next in the *We* sequence with $We = 34$, $q = 38$, and $Re = 6.7 \times 10^6$. This case uses the 0.5 mm nozzle. Figures 16, 17 shows fairly standard mixed mode breakup. Case 7 ($We = 40$, $q = 40$ and $Re = 7.5 \times 10^6$, Fig. 18) does as well but the increased *We* causes more vigorous aerodynamic stripping and what appears to be more rapid secondary breakup (producing a more dense cloud of droplets). Here, it is necessary to emphasize that because the images contain results for various nozzle sizes but within a fixed field of view, one must be careful to interpret the images while noting the nozzle size (and perhaps scaling the image appropriately if one intends to use images from the database).

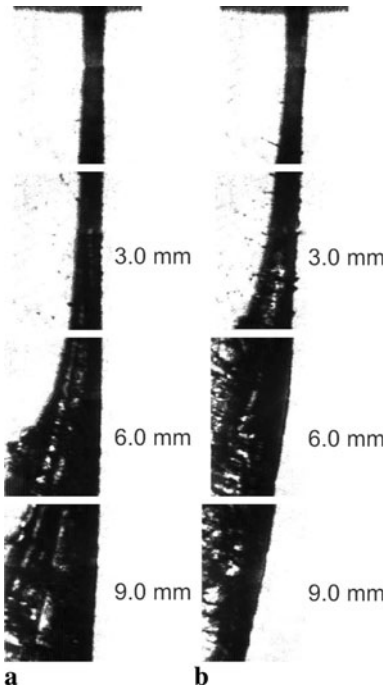

Fig. 15 Ballistic images of **a** case 4 ($We = 29$, $q = 153$, $Re = 1.5 \times 10^7$, $d_j = 0.7$ mm), and **b** case 3 ($We = 68$, $q = 64$, $Re = 1.5 \times 10^7$, $d_j = 0.7$ mm). Numbers provided on the right hand side of each composite image indicate vertical distance the spray system was raised (beam lower in the spray) relative to the position at the nozzle

As before, cases 8 and 7 depict fairly standard mixed mode breakup, but the higher *We* for case 7 causes more vigorous aerodynamic stripping. Again, no cloud of small droplets is evident here.

Case 6 (Fig. 19) uses a larger nozzle (1 mm) but lower gas velocity to achieve the same *We* as case 7. This produces $q = 153$ and $Re = 2.1 \times 10^7$ (the largest *Re* in this data set). Here, the breakup process is clearly transitioning away from bag/membrane breakup and beginning to show evidence of more vigorous stripping. Note that this transition is consistent with the work of Wu et al. and Faeth et al. Note also that the windward surface waves have a wavelength smaller than the jet diameter (in the Kelvin–Helmholtz regime) and pinch-off is less distinct with smaller structures, which is also consistent with other observations. Case 1 (using the 0.5 mm nozzle, $We = 49$, $q = 64$ and $Re = 1.1 \times 10^7$, Fig. 20) emphasizes this trend. Because the *We* is slightly higher but q much lower, one can observe the onset of surface stripping much closer to the nozzle.

The breakup process for case 6 is transitioning away from bag/membrane breakup and beginning to show evidence of more vigorous stripping in the shadowgrams. The droplet field is not visible in Fig. 21a, but leeward ligaments characteristic of stripping can be seen. Case 1

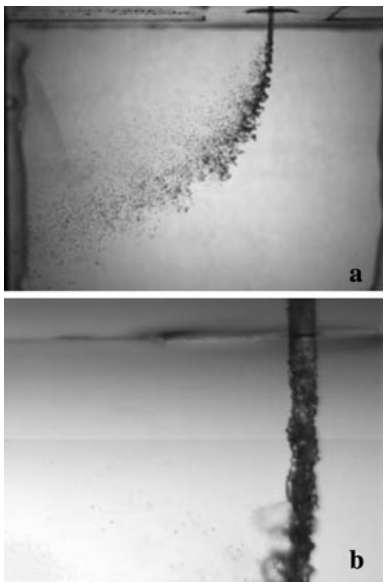

Fig. 16 Shadowgrams of the jet in Case 8 ($We = 34$, $q = 38$, $Re = 6.7 \times 10^6$, $d_j = 0.5$ mm). **a** Zoomed out to see the spray trajectory, **b** zoomed in right at the nozzle exit. Note, a symmetric shadow of the jet is cast above the nozzle orifice in the images; this should not be interpreted as a continuous jet extending to the top of the image

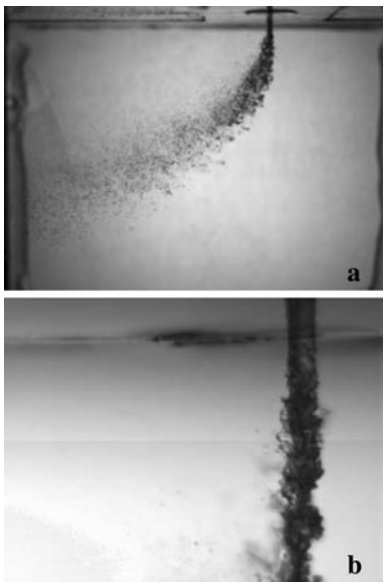

Fig. 18 Shadowgrams of the jet in Case 7 ($We = 40$, $q = 40$, $Re = 7.5 \times 10^6$, $d_j = 0.5$ mm). **a** Zoomed out to see the spray trajectory, **b** zoomed in right at the nozzle exit. Note, a symmetric shadow of the jet is cast above the nozzle orifice in the images; this should not be interpreted as a continuous jet extending to the top of the image

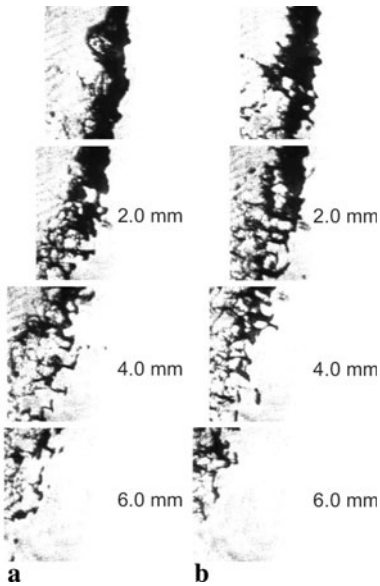

Fig. 17 Ballistic images of **a** case 8 ($We = 34$, $q = 38$, $Re = 6.7 \times 10^6$, $d_j = 0.5$ mm), and **b** case 7 ($We = 40$, $q = 40$, $Re = 7.5 \times 10^6$, $d_j = 0.5$ mm). Numbers provided on the right hand side of each composite image indicate vertical distance the spray system was raised (beam lower in the spray) relative to the position at the nozzle

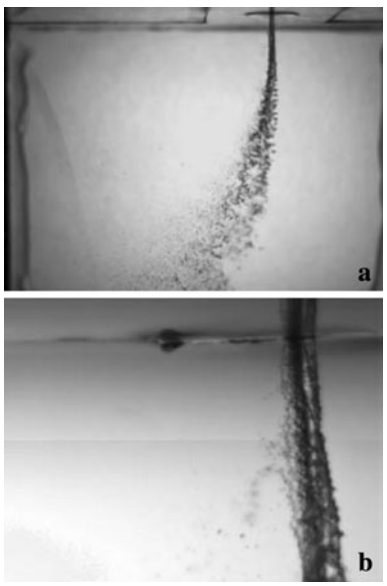

Fig. 19 Shadowgrams of the jet in Case 6 ($We = 41$, $q = 153$, $Re = 2.1 \times 10^7$, $d_j = 1.0$ mm). **a** Zoomed out to see the spray trajectory, **b** zoomed in right at the nozzle exit. Note, a symmetric shadow of the jet is cast above the nozzle orifice in the images; this should not be interpreted as a continuous jet extending to the top of the image

(Fig. 21b) emphasizes this trend. Because the We is slightly higher but q much lower, one can observe the onset of surface stripping and gas entrainment much closer to the nozzle.

Cases 5 and 10 use large nozzles (1 and 1.25 mm, respectively) to achieve higher We. Figure 22 shows case 5 with $We = 98$, $q = 64$, and $Re = 2.1 \times 10^7$. This jet demonstrates that there are flow cases where the jet is

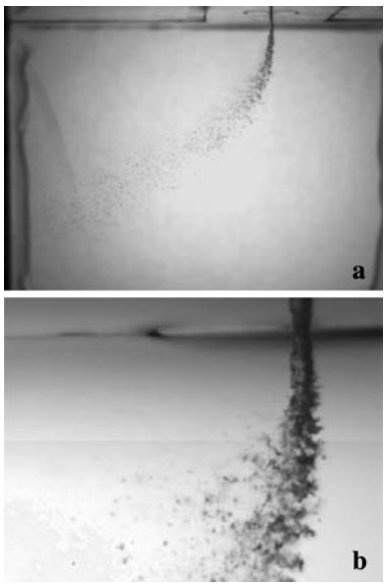

Fig. 20 Shadowgrams of the jet in case 1 ($We = 49$, $q = 64$, $Re = 1.1 \times 10^7$, $d_j = 0.5$ mm). **a** Zoomed out to see the spray trajectory, **b** zoomed in right at the nozzle exit. Note, a symmetric shadow of the jet is cast above the nozzle orifice in the images; this should not be interpreted as a continuous jet extending to the top of the image

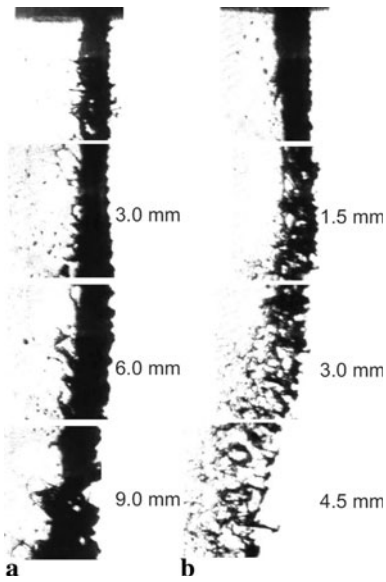

Fig. 21 Ballistic images of **a** case 6 ($We = 41$, $q = 153$, $Re = 2.1 \times 10^7$, $d_j = 1.0$ mm), and **b** case 1 ($We = 49$, $q = 64$, $Re = 1.1 \times 10^7$, $d_j = 0.5$ mm). Numbers provided on the right hand side of each composite image indicate vertical distance the spray system was raised (beam lower in the spray) relative to the position at the nozzle

affected by very early interactions that can not be controlled by the crossflow. In this case, the liquid column issues into the air looking very much like a free jet in the so-called "second wind" regime for jet breakup (Chigier and Reitz 1996). Indeed, several of the motion pictures depict a jet that develops over time, passing through mixed "sinuous" and "varicose" regimes before settling down to the image shown in Fig. 22b. Figure 23 contains corresponding images for case 10 ($We = 122$, $q = 64$ and $Re = 2.6 \times 10^7$). Here, the jet is atomizing more strongly owing to the high We, but the windward side of the near-field (Fig. 23b) is again free of longitudinal waves.

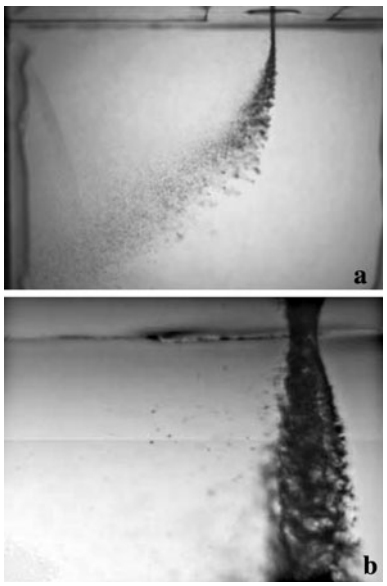

Fig. 22 Shadowgrams of the jet in case 5 ($We = 98$, $q = 64$, $Re = 2.1 \times 10^7$, $d_j = 1.0$ mm). **a** Zoomed out to see the spray trajectory, **b** zoomed in right at the nozzle exit. Note, a symmetric shadow of the jet is cast above the nozzle orifice in the images; this should not be interpreted as a continuous jet extending to the top of the image

Cases 5 and 10 (Fig. 24) use large nozzles to achieve high We. The shadowgrams are difficult to interpret for these cases, but when they are compared to the ballistic images, it is evident that the breakup occurs with small amounts of jet fluid, and one must conclude that surface stripping is dominant. Figures 25 and 26 and are included here in support of this interpretation, which is demonstrated more conclusively by examination of the full set of ballistic images for these cases. Again, the complete data set is available on request (contact the authors for instructions).

5 Image statistics

The shadowgrams make it possible to extract penetration lengths for the jets studied here and those are presented in Table 2.

The image analysis approach described in Sect. 3.4 was applied to the collection of ballistic images in the database to extract statistics on various features. The results

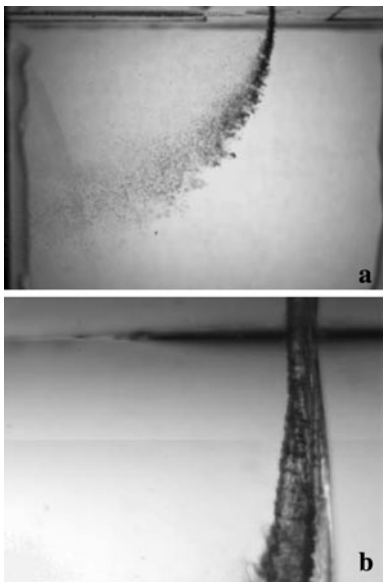

Fig. 23 Shadowgrams of the jet in case 10 ($We = 122$, $q = 64$, $Re = 2.6 \times 10^7$, $d_j = 1.25$ mm). **a** Zoomed out to see the spray trajectory, **b** zoomed in right at the nozzle exit. Note, a symmetric shadow of the jet is cast above the nozzle orifice in the images; this should not be interpreted as a continuous jet extending to the top of the image

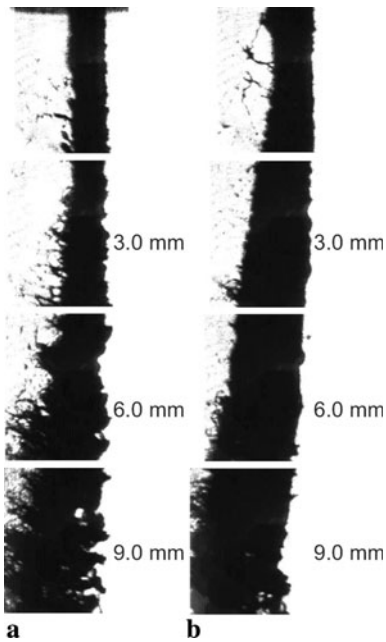

Fig. 24 Ballistic images of **a** Case 5 ($We = 98$, $q = 64$, $Re = 2.1 \times 10^7$, $d_j = 1.0$ mm), and **b** case 10 ($We = 122$, $q = 64$, $Re = 2.6 \times 10^7$, $d_j = 1.25$ mm). Numbers provided on the right hand side of each composite image indicate vertical distance the spray system was raised (beam lower in the spray) relative to the position at the nozzle

presented in Tables 2 to 3 represent the entire set of images for a particular flow case. Both the images and the Xflow code are available, however, if others prefer to analyze

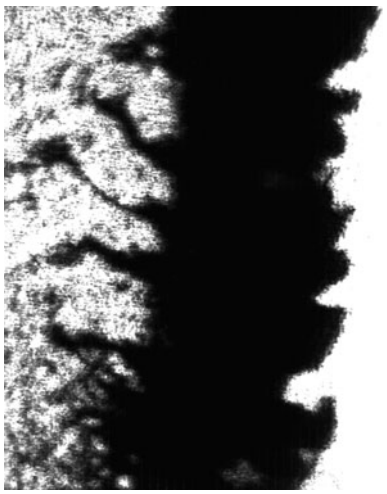

Fig. 25 Ballistic image of the jet in case 5 ($We = 98$, $q = 64$, $Re = 2.1 \times 10^7$, $d_j = 1.0$ mm), taken 9 mm below the nozzle orifice

Fig. 26 Ballistic image of the jet in case 10 ($We = 122$, $q = 64$, $Re = 2.6 \times 10^7$, $d_j = 1.25$ mm), taken 6 mm below the nozzle orifice

subsets of the data (e.g., to compare the very near-field to the downstream portions). Note that in Table 2, we report only on droplets that are larger than the spatial resolution of the instrument (about 20 μm here). If the size distribution we measure falls well above that cutoff, then we feel comfortable fitting a distribution to the data and presenting primary droplet statistics. Here, one can see that the SMD is on the order of 200 μm, which is an order of magnitude larger than the resolution cutoff. These are primary droplets located in the wake of the liquid column. Their size implies that they originate from column breakup. It is necessary, however, for users of this information to know that smaller droplets (caused by bag breakup, for example) were undoubtedly present but they are not reported in these statistics.

Table 2 Droplet and jet penetration statistics

We	Case	No. of droplets	Droplet mean diameter (μm)	Droplet Max. diameter (μm)	SMD (μm)	Penetration length (mm)
21	9	135 ± 52	140 ± 55	518 ± 270	160	9
21	2	227 ± 74	134 ± 52	504 ± 238	292	27
29	4	294 ± 131	101 ± 56	330 ± 253	272	27
34	8	109 ± 38	131 ± 59	483 ± 261	179	9
40	7	117 ± 50	155 ± 62	566 ± 265	165	12
41	6	145 ± 75	100 ± 75	270 ± 265	357	27
49	1	231 ± 59	107 ± 40	398 ± 197	289	15
68	3	212 ± 97	103 ± 51	373 ± 258	222	18
98	5	183 ± 84	97 ± 54	268 ± 218	217	21
122	10	46 ± 27	69 ± 64	134 ± 192	150	18

Table 3 Ligament, spatial wavelength, and void statistics

We	Case	No. of ligaments	Average Max. ligament length (μm)	Average Max. wavelength (μm/cycle)	No. of voids diameter (μm)	Void mean diameter (μm)	Void Max.
21	9	23 ± 18	1,040 ± 300	390 ± 140	66 ± 25	64 ± 35	151 ± 117
21	2	19 ± 15	500 ± 1,400	480 ± 130	99 ± 44	52 ± 23	115 ± 88
29	4	41 ± 25	470 ± 200	350 ± 150	229 ± 95	92 ± 54	239 ± 199
34	8	13 ± 10	610 ± 230	440 ± 180	50 ± 23	79 ± 69	177 ± 156
40	7	21 ± 14	750 ± 360	470 ± 190	71 ± 23	69 ± 30	158 ± 105
41	6	28 ± 22	500 ± 230	240 ± 50	88 ± 55	109 ± 72	221 ± 186
49	1	25 ± 23	700 ± 220	440 ± 170	86 ± 38	57 ± 23	121 ± 76
68	3	31 ± 31	490 ± 240	370 ± 130	167 ± 61	82 ± 42	226 ± 169
98	5	47 ± 24	800 ± 290	410 ± 120	105 ± 51	105 ± 59	232 ± 199
122	10	19 ± 18	600 ± 250	660 ± 210	52 ± 27	121 ± 72	243 ± 197

Equation 4 was presented by Sallam et al. (2004) as a correlation between the wavelength of the longitudinal waves (as observed from the images) and the Weber number. Here, we use Xflow to fit a curve to the shape of the leading (windward) edge of the column (because it bends), and then extract the surface features relative to that fit. We then perform FFTs on the features to find characteristic wavelengths. Maximum wavelengths are presented in Table 3. When we use these data together with the values for *We* in Table 1, we find that the correlation in Eq. 4 does not hold. Even the trends represented by Eq. 4 do not hold for our data. While our breakup regimes do match the regime map of Sallam et al., finer details are different. This highlights the fact that while the Weber number is one parameter affecting column breakup, it is not the only one. Various factors interact (e.g., interior flows or the effect of wind speed by itself on cases 3 and 4) and so it is not possible to use just one non-dimensional number to describe this jet in full.

6 Conclusions

In this work we have introduced and discussed the initial image data for a validation data set for liquid jets in crossflow. While much of our data agree with the literature, some finer details are different. The database is available for model developers to use. They need simply request information from the authors.

Future experiments will include droplet measurement in the dilute region via PDA and a move to other liquids with different fluid properties. In the longer term, the high-pressure rig at the Lund Institute of Technology can be fitted with a similar spray and the experiments repeated at 10 bar. Before much more work progresses, however, it is our hope that model developers can assess the data set and offer advice on what architectures and measurements are most useful. As one example, the secondary effects that seem to make our data different from others (cases 3 and 4 especially) provide interesting results but it may be more useful for model developers if we were to use a different

fluid nozzle, for example. Such a change would require revisiting the experiments described herein.

Acknowledgments Dr. Sedarsky was supported by the Swedish Research Council grant no. 621-2004-5504 and Air Force EOARD grant no. FA8655-06-1-3031. Dr. Paciaroni was supported by the Swedish Energy Agency and Dr. Berrocal has been financed by the Swedish Foundation for Strategic Research, both postdoctoral fellowships through the Centre for Combustion Science and Technology.

References

Bachalo WD (2000) Spray diagnostics for the twenty-first century. At Sprays 10(3–5):439–474

Bellofiore A, Cavaliere A, Ragucci R (2008) Piv characterization of sprays generated by crossflow injection in high-density airflow. In: Proceedings ILASS-Europe 2008, ILASS

Berrocal E (2006) Multiple scattering of light in optical diagnostics of dense sprays and other complex turbid media. PhD thesis, Cranfield University, Cranfield

Berrocal E, Kristensson E, Richter M, Linne MA, Aldén M (2008) Application of structured illumination for multiple scattering suppression in planar laser imaging of dense sprays. Opt Express 16(22):17870–17881

Cavaliere A, Ragucci R, Noviello C (2003) Bending and break-up of a liquid jet in a high pressure airflow. Exp Therm Fluid Sci 27:449–454

Chen TH, Smith CR, Schommer DG (1993) Multi-zone behavior of transverse liquid jet in high-speed flow. In: Proceedings 31st AIAA aerospace sciences meeting, AIAA

Chigier N, Reitz RD (1996) Recent advances in spray combustion: spray atomization and drop burning phenomena, Progress in Astronautics and Aeronautics, vol ~ 1, Reston, pp 109–135

Dunsby C, French PMW (2003) Techniques for depth-resolved imaging through turbid media including coherence-gated imaging. J Phys D Appl Phys 36(14):R207–R227

Freitag S, Hassa C (2008) Spray characteristics of a kerosene jet in cross flow of air at elevated pressure. In: Proceedings ILASS-Europe 2008, ILASS

Greenhaulgh DA, Jermy M (2002) Laser diagnostics for droplet measurements for the study of fuel injection and mixing in gas turbines and IC engines. In: Applied combustion diagnostics. Taylor and Francis, New York

Leong MY, McDonell VG, Samuelsen GS (2000) Mixing of an airblast-atomized fuel spray injected into a crossflow of air. NASA Glenn Research Center Report NASA/CR-2000-210467

Linne MA, Paciaroni ME, Gord JR, Meyer TR (2005) Ballistic imaging of the liquid core for a steady jet in crossflow. Appl Opt 44:6627–6634

Linne MA, Paciaroni ME, Hall T, Parker T (2006) Ballistic imaging of the near field in a diesel spray. Exp Fluids 40(6):836–846

Linne MA, Paciaroni ME, Berrocal E, Sedarsky DL (2009) Ballistic imaging of liquid breakup processes in dense sprays. Proc Combust Inst 32:2147–2161

Madabhushi RK (2003) A model for numerical simulation of breakup of a liquid jet in crossflow. At Sprays 13:413–424

Madabhushi RK, Leong MY, Hautman DJ (2004) Simulation of the breakup of a liquid jet in crossflow at atmospheric conditions. In: Proceedings of the ASME Turbo Expo 2004, ASME, Vienna

Mazallon J, Dai Z, Faeth GM (1999) Primary breakup of nonturbulent round liquid jets in gas crossflows. At Sprays 9:291–311

Otsu N (1979) A threshold selection method from gray-level histograms. IEEE Trans Syst Man Cybern 9(1):62–66

Paciaroni ME (2004) Time-gated ballistic imaging through scattering media with applications to liquid spray combustion. PhD thesis, Division of Engineering, Colorado School of Mines, Golden

Paciaroni ME, Linne MA (2004) Single-shot two-dimensional ballistic imaging through scattering media. Appl Opt 43:5100–5109

Paciaroni ME, Hall T, Delplanque JP, Parker T, Linne MA (2006) Single-shot two-dimensional ballistic imaging of the liquid core in an atomizing spray. At Sprays 16:51–70

Parker TE, Rainaldi LR, Rawlins WT (1998) A comparative study of room-temperature and combusting fuel sprays near the injector tip using infrared laser diagnostics. At Sprays 8:565–600

Rachner M, Becker J, Hassa C, Doerr T (2002) Modelling of the atomization of plain liquid fuel jet in crossflow at gas turbine conditions. Aerosp Sci Technol 6:495–506

Ragucci BR, Cavaliere A (2007) Trajectory and momentum coherence breakdown of a liquid jet in high-density air cross-flow. At Sprays 17:47–70

Reitz RD, Rutland CJ (1995) Development and testing of diesel engine cfd models. Prog Energy Combust Sci 21(2):173–196

Reynolds WC, Parekh DE, Juvet PJD, Lee MJD (2003) Bifurcating and blooming jets. Ann Rev Fluid Mech 35:295–315

Salewski M (2006) Les of jets and sprays injected into crossflow. PhD thesis, Division of Fluid Mechanics, Lund Institute of Technology, Lund

Salewski M, Stankovic D, Fuchs L (2008) Mixing in circular and non-circular jets in crossflow. Flow Turbul Combust 80:255–283

Sallam KA, Aalburg C, Faeth GM (2004) Breakup of round nonturbulent liquid jets in gaseous crossflow. AIAA J 42(12):2529–2540

Settles G (2001) Schlieren and shadowgraph techniques. Springer, Berlin

Wu PK, Kirkendall KA, Fuller RP, Nejad AS (1997) Breakup process of liquid jets in subsonic crossflows. J Propuls Power 13:64–73

Wu PK, Kirkendall KA, Fuller RP, Nejad AS (1998) Spray structures of liquid jets atomized in subsonic crossflows. J Propuls Power 14:173–182